

14 Unconventional Superconductivity in the Dynamical Vertex Approximation

Karsten Held

Institute for Solid State Physics, TU Wien

1040 Wien, Austria

Contents

1	Introduction	2
2	Dynamical vertex approximation	5
3	Ladder dynamical vertex approximation	10
4	Hubbard model, cuprates and nickelates	11
5	Spin fluctuations	15
6	Superconductivity	20
7	Conclusion and outlook	23

1 Introduction

With the success of dynamical mean-field theory (DMFT) [1–4] in calculating strongly correlated electron systems, there have been attempts from the very beginning [5] to systematically extend DMFT. The aim of such extensions is to keep the good description of DMFT for local electronic correlations, but at the same time also to capture non-local correlations beyond.

Indeed, the local DMFT correlations are doing an excellent job in describing a quasiparticle renormalization with a weight Z that is uniform in momentum space—a surprisingly good approximation for many transition metal-oxides and heavy fermion systems; as well as the Mott-Hubbard metal-insulator transition that emerges for $Z \rightarrow 0$ [2]. Furthermore, all kinds of orders (magnetic, orbital, charge density wave...) are quite well captured in three-dimensional systems up to the vicinity of the phase transition. Here, close to the phase transition, the mean-field nature of DMFT surfaces, among others, in the form of mean-field critical exponents. Non-local correlations are here essential for describing the proper critical behavior. With a diverging correlation length, long-range correlations feed back to the self-energy which thus becomes non-local.

The DMFT approach has been covered already in various other chapters of this Autumn School [3], and the present chapter will thus focus instead on non-local electronic correlations beyond DMFT. When are such non-local correlations important?

A lot of our insight into physical phenomena stems from weak coupling perturbation theory. Even though such an approach is certainly not applicable to strongly correlated electron systems, it often nonetheless provides for some qualitative understanding. One example, where non-local correlations enter the self-energy are spin-fluctuations. These can be calculated at weak coupling in the random phase approximation (RPA) which is discussed in quantum field theory textbooks. The RPA is the geometric series of all ladder diagrams with no, one, two etc. Coulomb interaction lines, as illustrated in Fig. 1 (top). The figure just shows one term of the sum, where “...” indicates that all orders in U are included. The RPA can be used to calculate the magnetic susceptibility Fig. 1 (top, without dashed line). As we will see later, the poles of this susceptibility constitute bosonic quasiparticle excitations coined magnons or, in the paramagnetic phase, paramagnons.

Now, when we add the dashed black line in Fig. 1 (top), we obtain a self-energy Feynman diagram. It describes the coupling of the electron to the spin-fluctuations. We can also call it the electron-(para)magnon interaction. As spin-fluctuations are very non-local we get—whenever spin-fluctuations become important—contributions from diagrams with lattice sites $i \neq j \neq k$ in Fig. 1 (top). Such self-energy diagrams are certainly not contained in DMFT, which sums up all *local* contributions of Feynman diagrams for the self-energy. Hence, whenever spin-fluctuations become large, we must expect important corrections to the DMFT self-energy. Indeed this is not restricted to spin-fluctuations, but depending on what kind of spin combination the particle and the hole in the RPA ladder have, one can also obtain the coupling of electrons to charge, orbital etc. fluctuations.

The present chapter is an updated version of the author’s lecture note at the Jülich Autumn School 2022 [4].

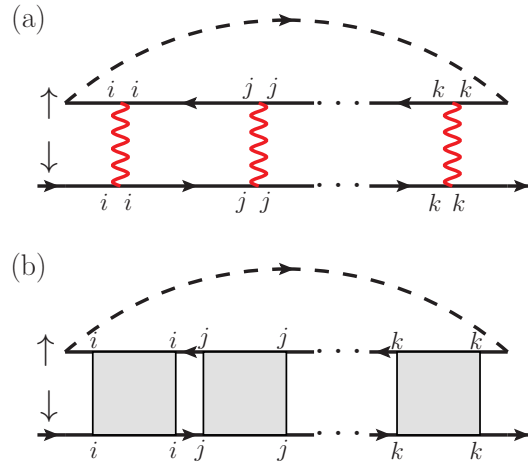


Fig. 1: *Top: Feedback of spin fluctuations (paramagnons) calculated in RPA to the self-energy. Bottom: In diagrammatic extensions of DMFT such physics is taken into account but with the bare interaction U (red wiggled line) replaced by a local vertex calculated from an impurity model (light gray box). Depending on the flavor of the diagrammatic extension of DMFT different local vertices are employed. Reproduced from [6].*

That means non-local correlations are certainly relevant whenever spin, charge etc. fluctuations are important. An obvious regime where this is the case is the vicinity of a second-order phase transition as already mentioned. Here the magnetic, charge etc. susceptibility diverges and significant changes to the DMFT solution are thus to be expected. For low dimensional systems we will get corrections also further away from the phase transition. The Mermin-Wagner theorem prohibits long-range order with a continuous symmetry breaking in two-dimensions at finite temperature. Hence, antiferromagnetic order is restricted to zero temperature. However, above this zero-temperature antiferromagnetic phase, we have now strong antiferromagnetic fluctuations in a wide temperature range, even with exponentially large correlation lengths. DMFT has been developed with the limit of dimension $d = \infty$ in mind, see [1] and Chapter “Understanding Correlated Materials with Lattice Fermions in Infinite Dimensions” by D. Vollhardt [3]. Hence, also from this perspective it is not surprising that we need to expect larger corrections to DMFT for low dimensional systems.

On the other hand, we would like to keep the success of DMFT in describing a major part of electronic correlations rather well: the local correlations. Two major routes to do so have been developed to this end. These are illustrated in Fig. 2: (i) Cluster extensions of DMFT [7] put the DMFT concept of locality onto a cluster (instead of a single site). This cluster is then embedded in a DMFT bath. For a single site cluster this is just DMFT. Illustrated in Fig. 2 is a two-site cluster where thus non-local correlations between the two red sites of the cluster are captured. Such two site clusters can, e.g., describe the formation of a spin singlet between two electrons on the two sites. For a four site cluster also d -wave superconductivity can be described. However such small clusters tend, in practice, to largely overestimate the physics that is compatible with the cluster such as the spin singlet formation and d -wave superconductivity for a two and four site cluster, respectively. While one can go to clusters of size 10×10 , a proper finite size scaling remains challenging. This is even more true for realistic multi-orbital calculations that are restricted to a handful of sites.

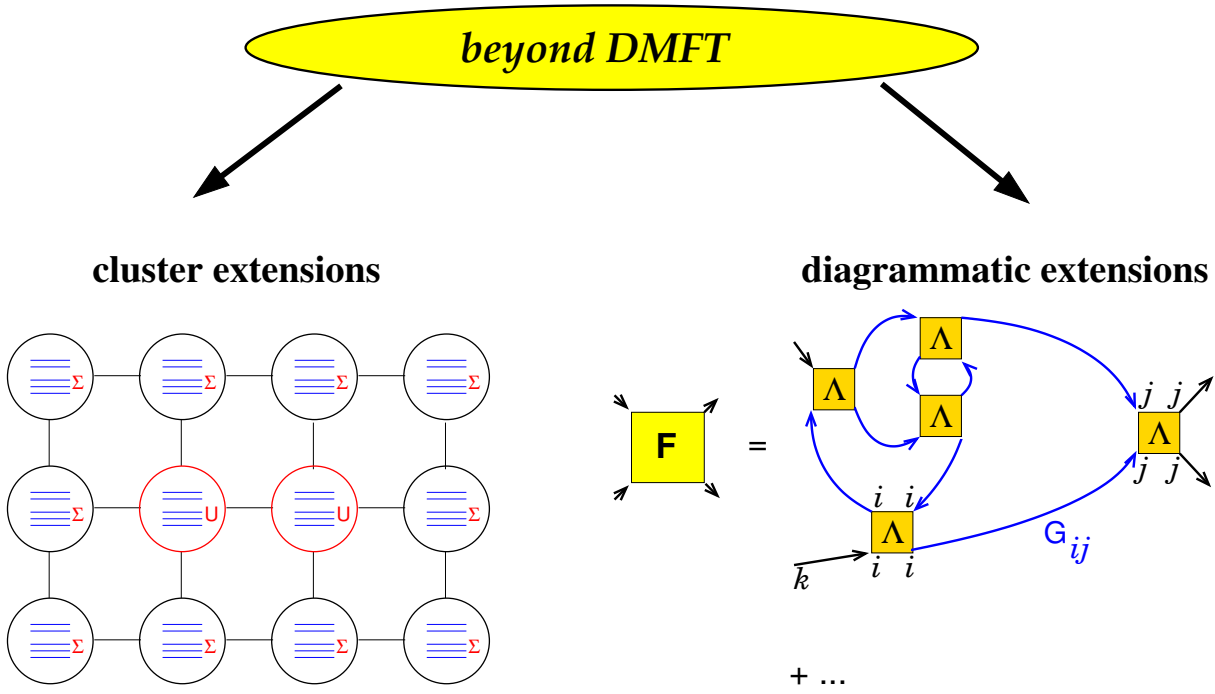


Fig. 2: *Left: In cluster extensions, a couple of sites (here two marked in red) are embedded in a dynamical mean field which can be formulated through the self energy Σ . Restricted to a single site, DMFT is obtained; extended to the full lattice the exact solution is recovered. Right: In diagrammatic extensions, the locality of DMFT is put to the next level, the two-particle level. Local two-particle building blocks Λ are connected by non-local Green function lines G_{ij} , resulting in a non-local full vertex F or susceptibility χ . When restricting G_{ij} to its local contribution G_{ii} , DMFT is recovered. Adapted from [8].*

The other route extends DMFT [6] Feynman diagrammatically. Here, the concept of locality is not extended to a cluster but instead to the n -particle vertex. For $n = 1$ we have the one-particle vertex which is nothing but the self-energy. And a local self-energy is just the DMFT approximation. For $n = 2$, i.e., the two-particle level, we start instead with a local two-particle vertex and construct from it the non-local full vertex F , see Fig. 2 (right), as well as the non-local self-energy and Green function. This is the level most commonly applied nowadays. Similarly as for the cluster extensions there are different flavors depending on which local vertex and which connecting Green functions are taken. At the end of the day, most of these different flavors are very similar, at least as long as they take the two-particle, four-point vertex as a starting point. Other approaches start from a three-point local vertex which is a more severe approximation. For an overview and comparison, see the review [6].

The originary method, called dynamical vertex approximation (D Γ A) [9], considers the vertex in terms of real fermions as local. A second widely applied approach is the dual fermion (DF) approach [10] which is covered in the Chapter “Path Integrals and Dual Particles” by A. Lichtenstein [3]. Also within D Γ A different flavors are used. In its most complete form, the fully irreducible vertex Λ is approximated to be local. Then the parquet equations are needed to construct F and the self-energy Σ . A local Λ is an excellent approximation, even for the two-dimensional Hubbard model in the superconducting doping regime [11]. In the ladder D Γ A

variant, the irreducible vertex Γ_ℓ in a certain channel ℓ such as the particle-hole (*ph*) channel is considered to be local. In this case, the Bethe-Salpeter equation is sufficient to calculate F along the same lines as in the RPA, only now with Γ_ℓ instead of U as a building block, i.e. the light gray box in Fig. 1 (bottom) is Γ_ℓ in this case. The ladder variant is numerically much less expensive. It is sufficient if a certain channel dominates, but does not capture the coupling of different channels into each other.

One can also extend the concept of locality to higher n -particle vertices. The $n=3$ -particle vertex level, for example, has been employed for estimating the error of the $n=2$ -particle calculations [12]. Correlation functions for $n=3$ or more particles are also relevant for non-linear response functions, and are thus naturally connected to $n=3$ -particle vertices [13]. For $n \rightarrow \infty$ the exact solution is recovered.

Turning back to Fig. 1, we see that such diagrammatic extensions are well suited to describe spin-fluctuations and their feedback to the fermionic self-energy. The same physics as is qualitatively described in RPA, is now captured for strongly correlated electrons since the local Λ already encodes non-perturbatively all DMFT correlations. The Bethe-Salpeter ladder of Fig. 1 is precisely the same as is also used to calculate the DMFT susceptibility, cf. the Chapter “DMFT for response functions” by E. Pavarini in 2022 [4]. What is not covered in DMFT is how these spin-fluctuations impact the self-energy as well as self-consistency effects, i.e., how the changed Σ modifies G or that the local Γ_ℓ itself becomes different from DMFT. These self-consistency effects lead to a dampening of the spin-fluctuations compared to the mean-field DMFT solution, up to the point of fulfilling the Mermin-Wagner theorem in two-dimensions.

Diagrammatic extensions of DMFT have been highly successful: (i) The critical behavior in the vicinity of (quantum) phase transition could be described for the first time in electronic models, a topic which was covered already excessively in the Autumn School 2018 [14], see also the review [6]. (ii) It was realized that the two-dimensional square lattice Hubbard model with perfect nesting is insulating all the way down to zero interaction [15], correcting earlier cluster DMFT results. (iii) The pseudogap and d -wave superconductivity can be described in the two-dimensional Hubbard model, a topic which we will cover in the following chapters. (iv) A new polariton, the π -ton has been discovered in model calculations [16]. (v) Realistic materials calculations are possible and have been pursued, e.g., for SrVO_3 [17].

In the following, we will first introduce one of the diagrammatic extensions of DMFT, the D Γ A, in Sec. 2. Simplifications when using the ladder variant of D Γ A are outlined in Sec. 3. The Hubbard model is introduced in Sec. 4 and its justification for cuprates and nickelates is discussed. Physical results regarding spin-fluctuations and superconductivity are discussed in Sec. 5 and 6, respectively. Finally, Sec. 7 provides a conclusion and outlook.

2 Dynamical vertex approximation

The aim of the present section is to provide the reader with the basic idea of the dynamical vertex approximation. It builds upon a similar chapter of a preceding Jülich Autumn School [14]. A more detailed description for a second reading can be found in the review [6]. Further

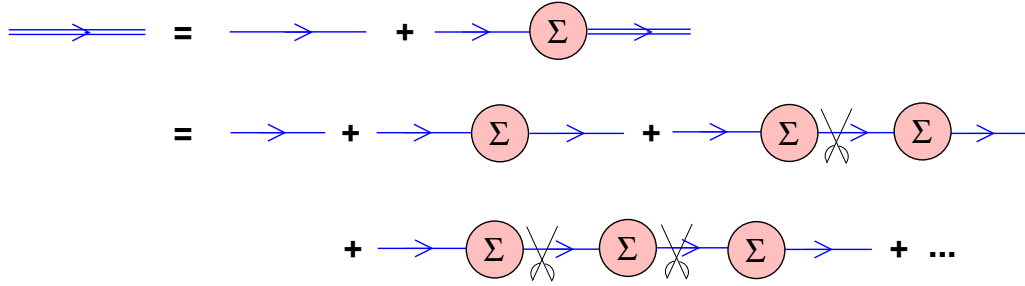


Fig. 3: Dyson equation connecting the Green function and self energy Σ (single blue line: non-interacting G_0 ; double blue line: interacting G). The pair of scissors indicates that these diagrams are one-particle reducible (i.e., cutting one G_0 line separates the Feynman diagram into two parts). From [14].

information on how to calculate the superconducting critical temperature T_c and how to include the asymptotic form of the vertex, can be found in [18].

The basic idea of the dynamical vertex approximation (D Γ A) is a resummation of Feynman diagrams, not order by order of the Coulomb interaction as in conventional perturbation theory, but in terms of their locality. That is, we assume the fully irreducible n -particle vertex to be local and from this building block we construct further diagrams and non-local correlations.

The first level ($n = 1$) is then just the DMFT which corresponds to all local Feynman diagrams for the self-energy Σ . Note that Σ is nothing but the fully irreducible $n=1$ -particle vertex. One particle-irreducibility here means that cutting one Green function line does not separate the Feynman diagram into two pieces. Indeed such reducible diagrams must not be included in the self-energy since it is exactly these diagrams that are generated from the Dyson equation (Fig. 3) which resolved for G reads

$$G_{\mathbf{k}\nu} = (1/G_{\mathbf{k}\nu}^0 - \Sigma_{\mathbf{k}\nu})^{-1} \quad (1)$$

for momentum \mathbf{k} , Matsubara frequency ν and non-interacting Green function $G_{\mathbf{k}\nu}^0$. In Fig. 3 and in the following, single blue lines denote non-interacting Green functions G_0 and double blue lines indicate interacting Green functions G . Fig. 3 further shows how one-particle reducible diagrams are generated through the Dyson equation. Hence these must not be contained in the Feynman diagrams that constitute Σ , to avoid a double counting. That means, Σ must be one-particle reducible in terms of G^0 .¹

On the next level, for $n = 2$, we assume the locality of the two-particle fully irreducible vertex Λ . For the two-particle vertex, fully irreducible means that cutting two Green function lines does not separate the diagram into two pieces. There are three different kinds (channels) ℓ of reducible vertices Φ_ℓ and a fourth, Λ , that is fully irreducible. Most importantly each diagram falls in one and only one of those four subgroups. Thus the full vertex F , containing all diagrams, can be written as the sum those. This decomposition of the vertex is called *parquet decomposition* and is graphically displayed in Fig. 4.

¹In terms of G the skeleton diagrams for Σ are also two-particle reducible. But that is another story that is connected with the way how Σ enters G .

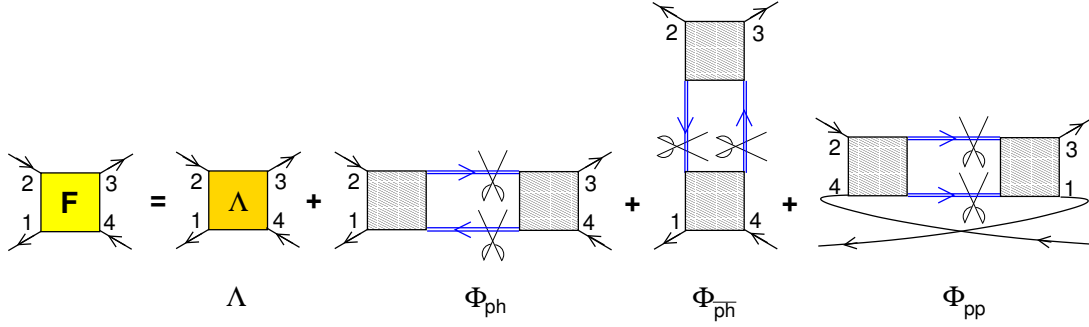


Fig. 4: Parquet decomposition of the full (reducible) vertex F into the fully irreducible vertex Λ and two-particle reducible diagrams Φ_ℓ in the three channels. The two pairs of scissors indicate the reducibility of the three Φ_ℓ 's. Each two-fermion Feynman diagram belongs to one and only one of the three Φ_ℓ 's or to Λ .

The reason why there are three distinct reducible parts Φ_ℓ is that, say, leg 1 may stay connected with leg 2, 3, or 4 when cutting two Green function lines as indicated in Fig. 4. These three possible channels ℓ are denoted as particle-hole (ph), transversal particle-hole (\overline{ph}) and particle-particle (pp). The irreducible vertex of each channel is just the complement: $\Gamma_\ell = F - \Phi_\ell$. It is important to note that each reducible diagram is contained in one and only one of these channels. One can show this by contradiction: otherwise cutting lines in two channels would result in a diagram with one incoming and two outgoing lines, which is not possible because of the conservation of (fermionic) particles.

There is further a set of six exact equations, which is also called the “parquet equations” [19, 6] to the confusion of the common student. These six equations allow us to calculate from a given Λ the six quantities: full vertex F , self-energy Σ , Green function G and the three reducible vertices Φ_ℓ .

(1) The first equation is the actual parquet equation [Fig. 4, Eq. (2)]

$$F_{r, \mathbf{k} \mathbf{k}' \mathbf{q}}^{\nu \nu' \omega} = \Lambda_{r, \mathbf{k} \mathbf{k}' \mathbf{q}}^{\nu \nu' \omega} + \Phi_{ph, r, \mathbf{k} \mathbf{k}' \mathbf{q}}^{\nu \nu' \omega} + \Phi_{\overline{ph}, r, \mathbf{k} \mathbf{k}' \mathbf{q}}^{\nu \nu' \omega} + \Phi_{pp, r, \mathbf{k} \mathbf{k}' \mathbf{q}}^{\nu \nu' \omega} \quad (2)$$

where $r \in \{c, s\}$ is the symmetric/antisymmetric spin combination, i.e., $F_{c/s} = F_{\uparrow\uparrow} \pm F_{\uparrow\downarrow}$ and similarly for other vertices.² The name indicates that F_c and F_s give rise to the charge and spin-fluctuations, respectively.

(2-4) Three of the six “parquet” equations are the Bethe-Salpeter equation in the three channels ℓ . In [Fig. 5, Eq. (3)] we here only reproduce the $\ell = ph$ channel; again with $r \in \{c, s\}$ for a symmetric/antisymmetric spin combination³

$$F_{r, \mathbf{k} \mathbf{k}' \mathbf{q}}^{\nu \nu' \omega} = \Gamma_{r, ph, \mathbf{k} \mathbf{k}' \mathbf{q}}^{\nu \nu' \omega} + \sum_{\mathbf{k}_1 \nu_1} F_{r, \mathbf{k} \mathbf{k}_1 \mathbf{q}}^{\nu \nu_1 \omega} G_{\mathbf{k}_1 \nu_1} G_{(\mathbf{k}_1 + \mathbf{q})(\nu_1 + \omega)} \Gamma_{ph, r, \mathbf{k}_1 \mathbf{k}' \mathbf{q}}^{\nu_1 \nu' \omega} \quad (3)$$

²This assumes SU(2) symmetry, if this is broken altogether four spin combinations need to be taken into account.

³We implicitly assume a proper normalization of the momentum and Matsubara frequency sums, i.e., $\sum_{\mathbf{k}} \hat{=} \frac{1}{N_K} \sum_{\mathbf{k}}$ and $\sum_{\nu} \hat{=} \frac{1}{\beta} \sum_{\nu}$, where N_K is the number of momentum points and $\beta = 1/T$ the inverse temperature.

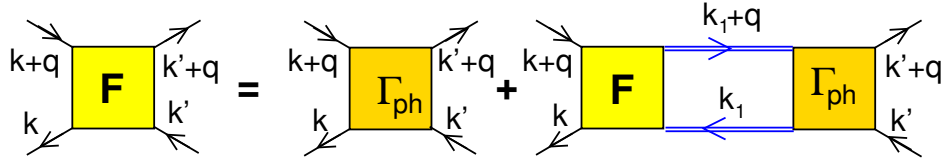


Fig. 5: Bethe-Salpeter equation in the particle-hole channel, $\ell = ph$, allowing us to calculate F from the irreducible vertex in Γ_{ph} in this channel. The rightmost term produces the particle-hole reducible diagrams denoted as Φ_{ph} in Fig. 4; $\Gamma_{ph} = \Lambda + \Phi_{ph}^- + \Phi_{pp}$.

One often combines frequency ν and momentum \mathbf{k} to a four vector $k = (\mathbf{k}, \nu)$. We do not do so in this chapter for the equations, but in the figures k represents (\mathbf{k}, ν) . Further it is important to choose a momentum-frequency convention for the vertices and stick to it. Because of energy and momentum conservation we only need three momenta and frequencies for the four points 1, 2, 3, 4 of the two-particle vertices in Fig. 4. Unless noted otherwise, we use the ph convention which is the natural one for the ph channel and already used in Fig. 5. That is, the 1, 2, 3, 4 frequency-momenta of Fig. 4 are related to Fig. 5 as follows: $k_1 = k$, $k_4 = k'$, $k_2 = k+q$, and—because of energy-momentum conservation— $k_3 = k'+q$. The Bethe-Salpeter equations in the other channels have the same structure just with another Γ_ℓ , $\ell = \overline{ph}$ or pp , and with another way to connect the building blocks (see Fig. 4). For these channels, there is another natural (diagonal) frequency-momentum q .

(5) The fifth equation is the Dyson equation that we already introduced [Fig. 3, Eq. (1)].

(6) Finally, the sixth equation is the Schwinger-Dyson equation [Fig. 6, Eq. (4)] which reads

$$\Sigma_{\mathbf{k}\nu} = \frac{Un}{2} - \frac{U}{2} \sum_{\mathbf{k}', q} \sum_{\nu', \omega} \left[F_{c, \mathbf{k}\mathbf{k}'\mathbf{q}}^{\nu\nu'\omega} - F_{s, \mathbf{k}\mathbf{k}'\mathbf{q}}^{\nu\nu'\omega} \right] G_{(\mathbf{k}+\mathbf{q})(\nu+\omega)} G_{\mathbf{k}'\nu'} G_{(\mathbf{k}'+\mathbf{q})(\nu'+\omega)} \quad (4)$$

and connects Σ and F . Here we consider a single-orbital and local interaction U that connects opposite spins. For this reason only $F_{\uparrow\downarrow} = (F_c - F_s)/2$ enters. The first term is simply the Hartree(-Fock) term, which is not included in Fig. 6 and where n is the average number of electrons per site in the paramagnetic phase.

This set of six exact parquet equations allows us to determine the six quantities F , Φ_ℓ , Σ , and G , as well as $\Gamma_\ell = F - \Phi_\ell$. If we knew the exact Λ , we could determine all of these quantities exactly, as well as associated one- and two-particle physics. Unfortunately, we do not know the exact Λ . Hence we need some approximation. If we approximate Λ by the bare Coulomb interaction U , we obtain the parquet approximation [19]. We can do better than this, and in D Γ A we approximate Λ by all local Feynman diagrams. Quantum Monte Carlo simulations show that this is an excellent approximation [11]. Indeed Λ is very compact. All two-particle reducible diagrams are generated from it and the first irreducible diagram that enters Λ besides the bare Coulomb interaction is of fourth order, see Fig. 7. So to speak the irreducible diagrams Λ form a skeleton from which many more diagrams are generated. Because of this, it is more local than Γ_ℓ and, in particular, much more local than F , Σ or G .

This local irreducible Λ is “summed up” in practice by solving an Anderson impurity model, similar as in DMFT but now we calculate the two-particle Green function of the impurity model and from this Λ . For example, we can use continuous-time quantum Monte Carlo simulations

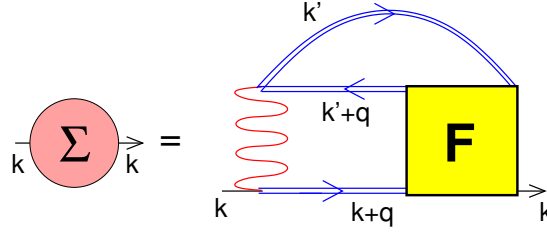


Fig. 6: Schwinger-Dyson equation connecting the full vertex F and the self-energy Σ .

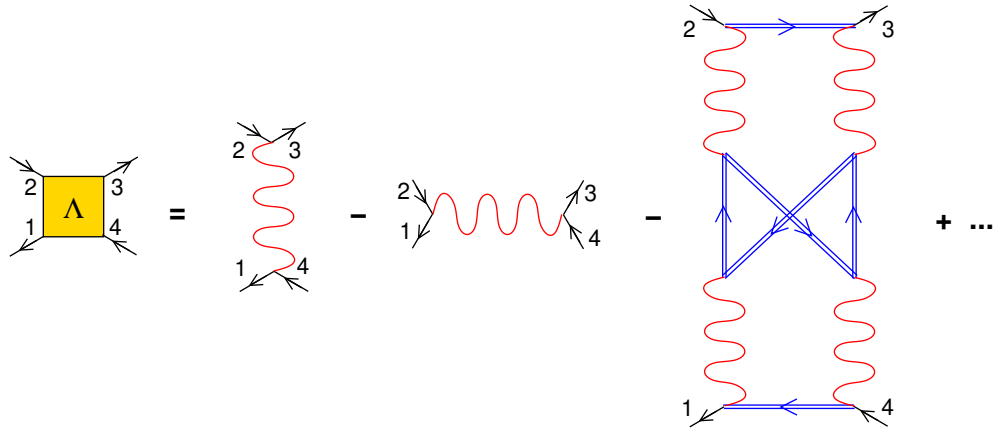


Fig. 7: Lowest order Feynman diagrams that contribute to the fully irreducible vertex Λ .

in the hybridization expansion see “QMC as a solver for DMFT” by P. Werner in 2022 [4], e.g., using the `w2dynamics` package [20] which allows us to calculate all two-particle responses using worm sampling [21].

In principle, one can then further turn to the $n=3$ -particle level etc.; and, for the $n \rightarrow \infty$ -particle fully irreducible local vertex $D\Gamma A$ one recovers the exact solution. As a matter of course determining the $n=3$ -particle vertex becomes already cumbersome. But it may serve at least as an error estimate [12] if one is truncating the scheme at the two-particle vertex level. Also completely new physics, that is hitherto not understood, may be hiding behind diagrams generated from the $n=3$ -particle irreducible vertex. Some physical processes such as Raman scattering and non-linear response naturally require three-particle vertex functions [13].

In the present section we have learned about the full-fledged parquet $D\Gamma A$. It is unbiased with respect to all three channels ℓ and thus treats antiferromagnetic or charge fluctuations in the ph -channel on a par with e.g., superconducting fluctuations or weak localization corrections in the pp channel. It also mixes the different channels. For two channels this mixing generates, with some fantasy, a traditional parquet floor like pattern with ladder rungs in one direction intermixed by ladder rungs in the orthogonal direction etc., hence the name. Being unbiased definitely is a great advantage. For example, in [16] we were looking for weak localization corrections to the optical conductivity in the pp channel and excitons that live in the ph channel. Instead we found that for strongly correlated systems that host strong alternating spin or charge fluctuations, the \overline{ph} channel is actually dominant for the optical conductivity, against all expectations.

The drawback of the full parquet solution is that we deal with three momenta and three frequencies. Even on a rather coarse discretization grid, we thus easily end up with terabytes of data. In the Bethe-Salpeter equation (3) the bosonic momentum \mathbf{q} and frequency ω decouple, so that it can be well distributed on several computer cores without the need to communicate. However, this natural \mathbf{q} and ω is channel-dependent (see [6]), i.e., different for the three channels of Fig. 4. Hence, when we add the three channels in the parquet equation (2), we mix different momenta, requiring a lot of communication between different computer cores, which, say, have previously solved the Bethe-Salpeter equation in different channels. Network traffic thus becomes the computational bottleneck on a supercomputer for parquet D Γ A. Efforts to mitigate this problem are the truncated unity basis for momentum space [22], the intermediate representation (IR) for frequency space [23], the single boson exchange decomposition [24], and quantum tensor trains which are covered in Chapter “Learning Feynman Diagrams with Tensor Trains” by X. Waintal [3].

3 Ladder dynamical vertex approximation

If we know that a certain channel is dominating, we can restrict ourselves to this particular channel and neglect the others and the mixing of different channels through the parquet equation. Since Φ_{ph} and $\Phi_{\overline{ph}}$ are related by crossing symmetry (invariance of exchanging the two incoming lines [6]) both of these channels contribute to F in the same way, albeit with a crossing-symmetry exchanged frequency and momentum combination. Hence, both channels must be included in general.⁴ In this case, we hence only need to solve the Bethe-Salpeter equation (3) and can consider a local Γ_{ph} as input. For a bare interaction U , the Bethe-Salpeter equation (3) yields diagrams as in Fig. 8(a). If we improve on this and use a local Γ_{ph} we get the ladder D Γ A approach and the diagrams of Fig. 8(b). From these diagrams (plus the contribution from the crossing-symmetrically related \overline{ph} channel) we get F , and from F in turn through the Schwinger-Dyson equation (4) the self-energy.

If we want to calculate superconducting fluctuations in ladder D Γ A we can plug the antiferromagnetic spin-fluctuations as a superconducting pairing glue (which is nothing but Γ_{pp}) into the pp channel. This is so-to-speak a poor man’s one-step parquet calculation. It mixes the ph and \overline{ph} channel into the pp (or Cooper) channel. That is, spin (and charge) fluctuations from the ph and \overline{ph} channels can induce superconductivity, but we do not feed back the pp fluctuations to the ph and \overline{ph} channel. For details on the superconducting calculations and also regarding the treatment of high frequencies, see [18].

A self-consistency with respect to the recalculation of the Green function entering the Bethe-Salpeter equation (3) is possible [25]. Different schemes have been proposed as well for a self-consistency with respect to Γ (or Λ) starting with [26], for an overview see [6]. A simpler

⁴When we eventually connect F with altogether four Green functions to a susceptibility with a single bosonic momentum and frequency [see Eq. (6) and Fig. 12 below], the $\mathbf{q} = (\pi, \pi, \dots)$ susceptibility is dominated in case of antiferromagnetic spin fluctuations by the ph channel, whereas the $\mathbf{q} = (0, 0, \dots)$ optical susceptibility (conductivity) is dominated by the transversal particle-hole channel (π -tons [16]).

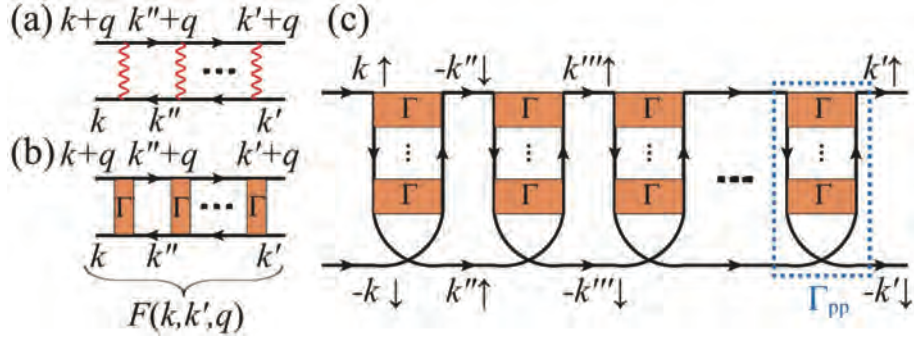


Fig. 8: (a) Spin-fluctuations as calculated from the Bethe-Salpeter ladder diagrams in terms of the bare Coulomb interaction U in RPA. (b) Same as (a) but now calculated in ladder DΓA from the local irreducible vertex in the ph channel: $\Gamma \equiv \Gamma_{ph}$. (c) These antiferromagnetic spin-fluctuations enter as Γ_{pp} (via the parquet equation) in the particle-particle channel. This leads to the binding of two electrons into a Cooper pair, and if this bosonic Cooper pair Bose-Einstein condensates to superconductivity. From [27].

and widely used approach is to do, instead, a so-called Moriyaesque λ -correction [6]. It essentially adds a mass to the paramagnons (dampens the antiferromagnetic spin fluctuations). This mass is fixed by a sum-rule for the susceptibility, and automatically ensures the correct high-frequency asymptotics of the self-energy. This λ -correction has been introduced to mimic the self-consistency and represents a considerable simplification of the calculations. For a further-going discussion see [6, 27].

The advantage of the ladder DΓA is that—as long as we do not couple the ladders through the parquet equations—the ladder only depends on a single frequency-momentum q instead of three (q, k, k') . Hence numerically much lower temperatures, larger frequency grids and finer momentum grids are feasible. Also realistic multi-orbital *ab initio* DΓA calculations are possible with the ladder DΓA version [17]. The results presented in the following have been obtained by ladder DΓA with a Moriyaesque λ -correction.

4 Hubbard model, cuprates and nickelates

In this chapter, we consider the one-band Hubbard model in two or three-dimensions

$$\mathcal{H} = - \sum_{ij, \sigma} t_{ij} c_{i\sigma}^\dagger c_{j\sigma} + U \sum_i n_{i\uparrow} n_{i\downarrow}. \quad (5)$$

It consists of two terms: (i) a hopping term t_{ij} between sites i and j , which we restrict in the following to a nearest neighbor t , next-nearest neighbor t' and next-next-nearest neighbor t'' ; and (ii) a local Coulomb repulsion U . Here $c_{i\sigma}^\dagger$ ($c_{i\sigma}$) creates (annihilates) an electron on site i with spin σ in second quantization and $n_{i\sigma} = c_{i\sigma}^\dagger c_{i\sigma}$.

The Hubbard model is the quintessential model for strongly correlated electron systems, similar as the Ising model for statistical physics or the drosophila fly for genetics. For $t_{ij} = 0$, we have just a collection of atoms and a spectra with peaks at $\pm U/2$ for half-filling. For $U = 0$, there is no interaction and we can solve the tight-binding Hamiltonian by Fourier transforming t_{ij} to $\varepsilon_{\mathbf{k}}$ in momentum space. Then, just occupying all single-particle states up to the Fermi

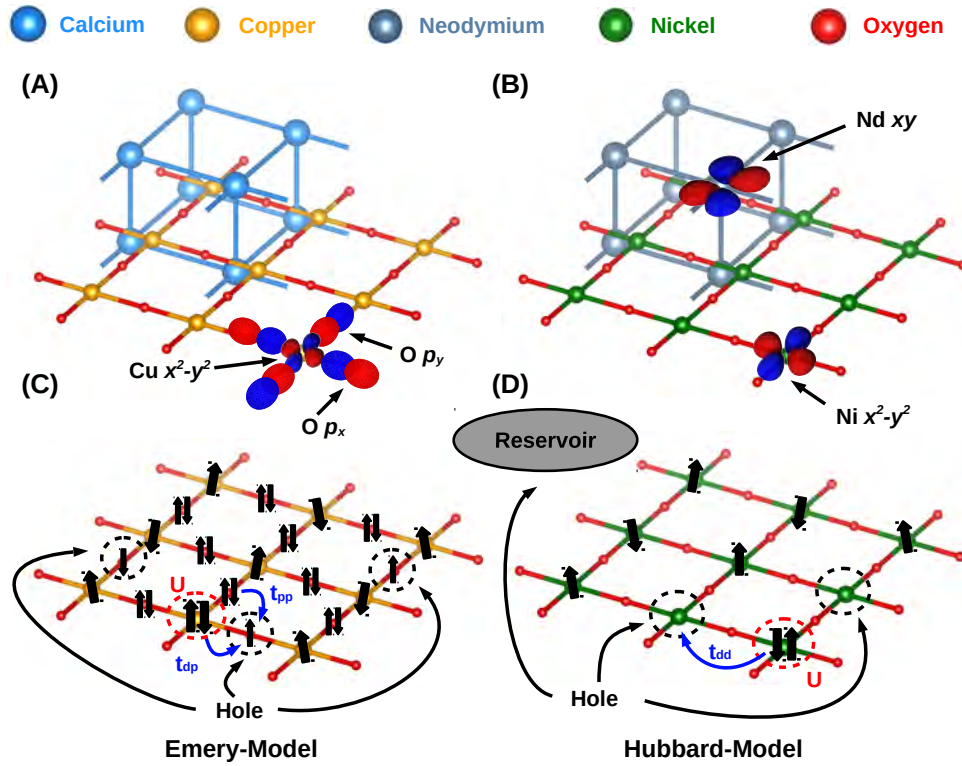


Fig. 9: Crystal structure of (A) a characteristic cuprate, CaCuO_2 , and (B) the nickelate NdNiO_2 . The $\text{Cu}(\text{Ni})\text{O}_2$ layers are separated by $\text{Ca}(\text{Nd})$ spacing layers in this “infinite-layer” structure. Also shown are the relevant low-energy orbitals in both cases. (C) Cuprates are charge transfer insulators so that the oxygen orbitals need to be included for an accurate microscopic description. The simplest such model is the **Emery model** with copper $3d_{x^2-y^2}$, oxygen p_x and p_y orbitals. As indicated there is a hopping t_{pd} between Cu and O sites, and further a hopping t_{pp} between O sites; double occupations are suppressed by the interaction U on the Cu sites just as in the Hubbard model. (D) For nickelates we have a Ni - $3d_{x^2-y^2}$ -band and a A -pocket derived from the Nd $5d_{xy}$ band crossing the Fermi energy. Both are largely decoupled but we need to calculate, e.g., by DFT+DMFT, how many holes go into the Ni - $3d_{x^2-y^2}$ -band **Hubbard model** and how many go into the A -pocket **reservoir**. From [28].

energy gives the ground state. But, if we switch on U the electrons become correlated, the expectation value is correlated: $\langle n_{i\sigma} n_{j\sigma'} \rangle \neq \langle n_{i\sigma} \rangle \langle n_{j\sigma'} \rangle$, i.e., local double occupations $\langle n_{i\uparrow} n_{i\downarrow} \rangle$ are heavily reduced compared to the non-interacting, uncorrelated value on the right-hand-side of the equation.

While a screened interaction can—to a good approximation—often be replaced by the purely local interaction U , materials require typically the consideration of more bands than the single-band Hubbard model. This is even the case when we restrict ourselves to the low-energy orbitals around the Fermi energy. An important exception are cuprate and nickelate⁵ superconductors. For the Ruddlesden-Popper $\text{La}_3\text{Ni}_2\text{O}_7$ under pressure, critical temperatures are close to 100 K.

⁵Here, we refer to infinite-layer nickelates. More recently also superconducting Ruddlesden-Popper nickelates have been synthesized [29] which have a very different physics: (i) oxygen orbitals strongly connect a few NiO_2 layers making the system much more three dimensional; (ii) further these Ruddlesden-Popper nickelates have more than two holes in the Ni $3d$ orbitals so that multi-orbital physics is immanent.

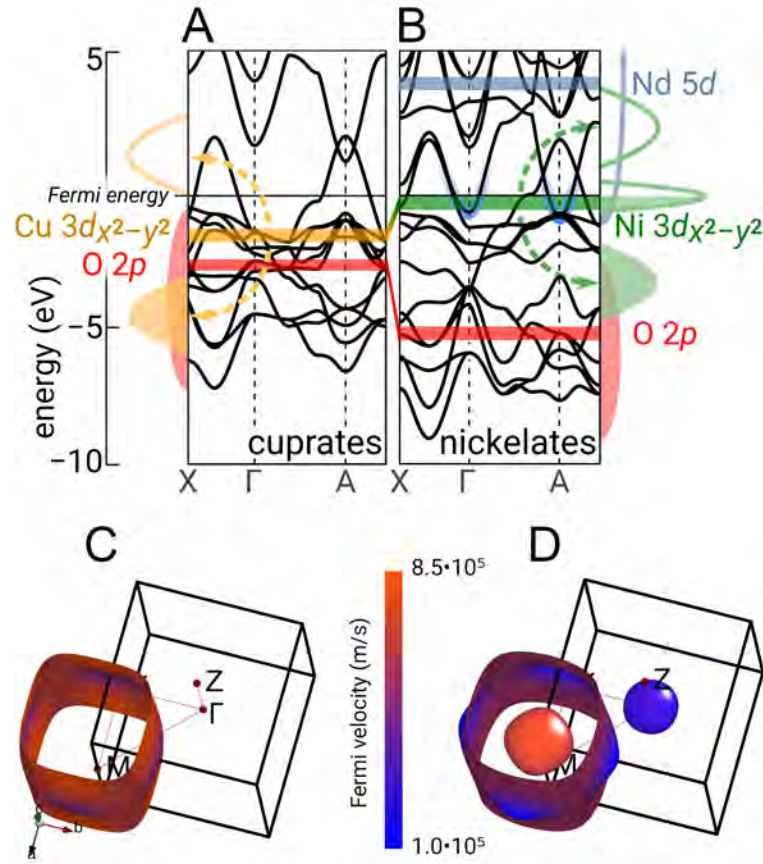


Fig. 10: (A,B) Electronic structures of (A) CaCuO_2 and (B) LaNiO_2 as calculated in DFT. The side panels indicate the effect of electronic correlations and the color bars the center of energy of the most important bands. (C) and (D) DFT Fermi surface corresponding to (A) and (B), respectively. From [28].

The arguably simplest cuprate and nickelate crystal structure is the “infinite-layer”⁶ structure displayed in Fig. 9(A) and (B). Since the valence of the spacer cations is Ca^{+2} and $\text{Nd}(\text{La})^{+3}$, the formal oxidation state is Cu^{+2} and Ni^{+1} , respectively, so that both cuprates and nickelates are in a formal $3d^9$ configuration. After such basic chemistry considerations, the first step to get an idea of the relevant orbitals is doing a density functional theory (DFT) calculation.

Fig. 10 shows that for the cuprates a single $3d_{x^2-y^2}$ -orbital is crossing the Fermi level. It gives rise to the single hole-like Fermi surface sheet displayed in the lower left panel of Fig. 10. This Cu $3d_{x^2-y^2}$ -band and Fermi surface can well be described with proper hopping parameters t , t' and t'' . But now we need to include the effect of electronic correlations. These are indicated by the dashed arrows and the side panels of Fig. 10(A): the Cu $3d_{x^2-y^2}$ -band splits into an upper and lower Hubbard band. Since the oxygen orbitals are just a few eV below the Fermi energy, these oxygen orbitals end up above the lower Hubbard band. As a consequence we have a charge transfer insulator according to the scheme of Zaanen-Sawatzky-Allen and not a Mott insulator, which one might have expected from the splitting into Hubbard bands. That is, if we dope cuprates, and we need to do so to have a superconductor, the holes go into the

⁶The two distinct layers displayed in Fig. 9 are repeated on top of each other ad infinitum.

oxygen bands. Hence, in the case of cuprates, an Emery model description which incorporates the copper $3d_{x^2-y^2}$ -band and oxygen p_x and p_y bands as visualized in Fig. 9(C) is the most appropriate low-energy model. Nonetheless, the majority of theoretical papers studying the cuprates use the single-band Hubbard model. This is to some extent justified by the fact that oxygen-hole spin and copper spin form a Zhang-Rice singlet, which can be described effectively by the Hubbard model. Also in experiment, there is a single Fermi surface as in Fig. 10(C) of mixed oxygen and copper character.

In case of the nickelates, these oxygen bands are instead at a considerably lower energy. Hence the lower Hubbard band is now above the oxygen band and we would have a Mott insulator, if it was not for the Nd(La) $4d$ -bands.⁷ These Nd(La) $4d$ bands are closer to the Ni $3d$ -bands than the unoccupied Ca and Cu s bands are to the Cu bands. They even cross the Fermi level around the Γ and A momentum, which leads to the formation of pockets around these momenta in DFT, see Fig. 10(D). The charge transferred to the Nd(La) pockets also leads to a self-doping of the Ni $3d_{x^2-y^2}$ -band: even the parent compound Nd(La)NiO₂ has about 0.05 holes per Ni. In such a situation, a quasi-particle peak develops as indicated in the side panel of Fig. 10(B) with a quasiparticle mass enhancement $m^*/m = 1/Z$ calculated to be about five for the undoped parent compound and about three at 20% Sr doping [30]. A further correlation effect is that the Γ -pocket is shifted above the Fermi level, at least for larger Sr-doping and for LaNiO₂.

Altogether this leaves us with two relevant bands as displayed in Fig. 9(B): the Ni $3d_{x^2-y^2}$ -band and the Nd(La)-derived A -pocket. Both bands do not hybridize and can hence, to a first approximation, be considered as decoupled. The expectation is that the more strongly correlated Ni $3d_{x^2-y^2}$ -band is responsible for the superconductivity. Using Occam's razor, i.e., if we try to identify the most simple model, we end up with a one-band Hubbard model for the Ni $3d_{x^2-y^2}$ -band and a decoupled reservoir (A -pocket) that must be taken into account for translating the Sr-doping of Nd(La)_{1-x}Sr_xNiO₂ into the actual hole doping of this Hubbard model. Otherwise the A -pocket is merely a passive bystander. This simple model is illustrated in Fig. 9(D).

The hopping parameters of the nickelate Hubbard model can be obtained from a Wannier function projection onto the Ni $3d_{x^2-y^2}$ -band: $t = 0.395$ eV, $t'/t = -0.25$, $t''/t = 0.12$ [30]. Further, the interaction strength U can be calculated by constrained random phase approximation (cRPA, see Chapter “Screened Coulomb Interactions from cRPA” by J.M. Tomczak [3]). Considering the fact that U is frequency(ω)-dependent in cRPA and—within the relevant energy range—on average slightly larger than $U(\omega=0)$, one obtains $U \approx 8t$ from cRPA. For further details see [30].

The translation from Sr-doping to the occupation of the $3d_{x^2-y^2}$ -band has been calculated in DFT+DMFT⁸ including all five Nd and all five Ni d bands in DMFT. Fig. 11 (blue curve) shows the results: One sees that roughly 50% of the holes (there is one hole per Sr) go into the $3d_{x^2-y^2}$ -band and the remaining 50% go into the pockets. For larger Sr-dopings, at around 25%,

⁷We here show LaNiO₂ since it is slightly easier to calculate than NdNiO₂ in DFT because it has no $4f$ -electrons. Experimentally, La_{1-x}Sr(Ca)_xNiO₂ is also a nickelate superconductor with a T_c comparable to NdNiO₂.

⁸For the DFT+DMFT method, see the Chapter “LDA+DMFT for strongly correlated materials” by A. Lichtenstein in 2022 [4]

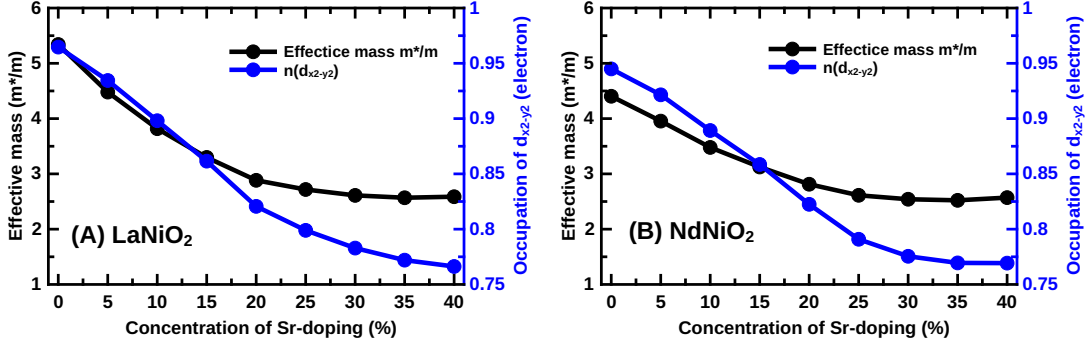


Fig. 11: Translation of Sr-doping to the occupation of the Ni $3d_{x^2-y^2}$ -band (blue line; right y-axis) and corresponding effective mass enhancement m^*/m (black line; left y-axis) as calculated by DFT+DMFT for (A) $\text{La}_{1-x}\text{Sr}_x\text{NiO}_2$ and (B) $\text{Nd}_{1-x}\text{Sr}_x\text{NiO}_2$. From [30] (Supplemental Material).

the curve flattens because here the Ni $3d_{3z^2-r^2}$ orbital approaches the Fermi level and accommodates holes as well. The one-band Hubbard model DMFT calculation gives a very similar spectrum as the full DFT+DMFT calculations with 5+5 Nd+Ni orbitals. Also the effective mass plotted in Fig. 11 (black curve) agrees [30]. Altogether this hints that the simple Hubbard model is a good approximation for nickelates; experimental results are also consistent with this picture as detailed below.

5 Spin fluctuations

Spin fluctuations as visualized in Fig. 8(a,b) enter the full vertex F but subsequently also the susceptibility which is connected to F as follows (Fig.12)

$$\chi_{r,\mathbf{q}\omega} = \underbrace{\sum_{\mathbf{k}\nu} G_{\mathbf{k}\nu} G_{(\mathbf{k}+\mathbf{q})(\nu+\omega)}}_{\equiv \chi_{\mathbf{q}\omega}^0} - \sum_{\mathbf{k}\mathbf{k}'\nu\nu'} G_{\mathbf{k}\nu} G_{(\mathbf{k}+\mathbf{q})(\nu+\omega)} F_{r,\mathbf{k}+\mathbf{k}'\mathbf{q}}^{\nu\nu'\omega} G_{\mathbf{k}'\nu'} G_{(\mathbf{k}'+\mathbf{q})(\nu'+\omega)} \quad (6)$$

for $r = c/s$, i.e., the spin and charge susceptibility, respectively. As before, we restrict ourselves to the paramagnetic phase for simplicity. The first term on the right hand side of Eq. (6) is just the bare bubble contribution χ^0 , obtained directly from two (interacting) Green function; the second term are vertex corrections calculated from F . The minus sign is a matter of definition of F . When F is calculated in RPA as in Fig. 8(a), we have $\Gamma_r = \pm U$ for $r = c/s$ and obtain a

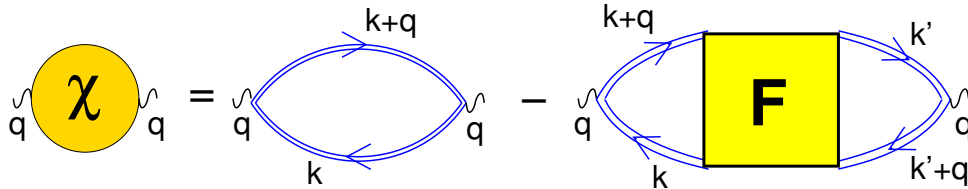


Fig. 12: The susceptibility χ consists of the bare bubble χ^0 (first term on the right hand side) and vertex corrections that can be calculated from the full vertex F .

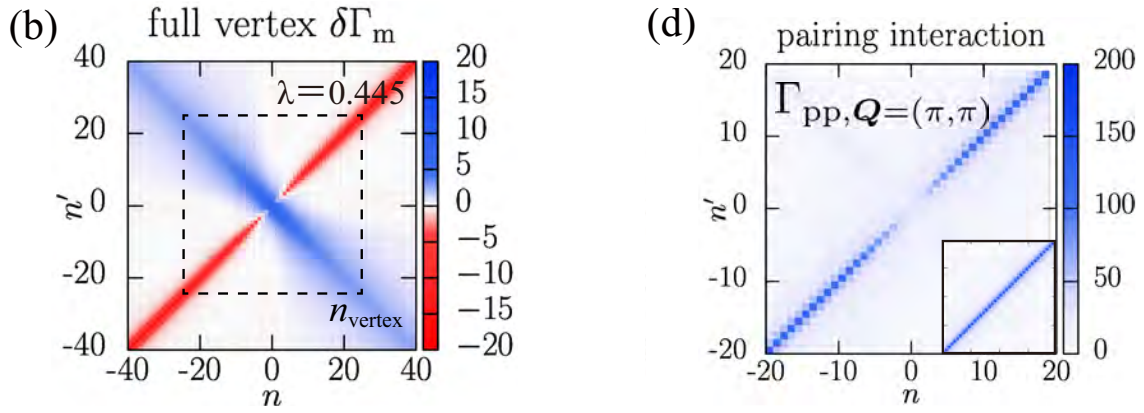


Fig. 13: Left: Difference of the local ph vertex in the magnetic channel from $-U$, i.e., $\delta\Gamma_m = \Gamma_s - (-U)$ vs. the two fermionic Matsubara frequencies $\nu_n = i(2n+1)\pi T$ and ν'_n at zero bosonic frequency $\omega = 0$. At small frequencies, $\Gamma_{s,ph}$ and associated spin-fluctuations are suppressed. Right: This suppression also leads to a suppression of the non-local pp vertex Γ_{pp} , i.e., the superconducting pairing glue, at small frequencies. It is obtained from antiferromagnetic spin fluctuations (i.e., from the local Γ_s corresponding to the left panel and the Bethe-Salpeter equation, see Sec. 6). Right inset: Γ_{pp} as calculated in RPA. From [27] where further details and parameters can be found.

geometric sum, which eventually yields

$$\chi_{r,q\omega}^{RPA} = \frac{\chi_{q\omega}^0}{1 \pm U\chi_{q\omega}^0} \quad (7)$$

where the \pm is for $r = c/s$. For certain ω 's and \mathbf{q} 's Eq. (7) develops poles. We call these bosonic excitations (para)magnons. The ω - \mathbf{q} energy-momentum dispersion relation of these quasiparticles follows the position of the poles.

The minus sign in Eq. (7) already indicates that spin-fluctuations are generally stronger in a Hubbard model. This can change if additional non-local interactions V are included. These trigger a transition from an antiferromagnetic spin to a charge density wave order for $\mathcal{Z}V > U$ in mean field (\mathcal{Z} : number of neighbors; V : nearest neighbor Coulomb repulsion). Which magnetic order dominates in RPA, solely depends on the \mathbf{q} for which $\chi_{\mathbf{q}\omega=0}^0$ is strongest. Close to half-filling, we often have Fermi surfaces where for a \mathbf{k} on the Fermi surface ($\nu=0$) also $\mathbf{k}+\mathbf{q} = (\pi, \pi, \dots)$ is at or close to the Fermi surface. Then both $G_{\mathbf{k}\nu=0}$ and $G_{(\mathbf{k}+(\pi,\pi,\dots))(\nu+\omega)=0}$ are large in Eq. (6), and the antiferromagnetic susceptibility $\chi_{\mathbf{q}=(\pi,\pi,\dots)\omega=0}^0$ is maximal. Of course, this is just the weak coupling picture. For larger Coulomb interactions we form large magnetic moments and the change of physics is reflected in vertex F corrections beyond RPA. More recently it could be demonstrated [27] that the local vertex $\Gamma_{r=m}$ is suppressed compared to the RPA value $\Gamma_s = -U$. This is shown in Fig. 13 (left). This suppression, in particular that at the relevant small frequencies, leads to reduced spin-fluctuations. Consequently, the superconducting pairing as calculated along the line of Fig. 8(b,c) is suppressed as well, see Fig. 13 (right). The origin of the suppression of Γ_s at small frequencies are local particle-particle excitations that enter Γ_s . These reduce Γ_s along the side diagonal frequencies $\nu = -\nu'$. In the literature such particle-particle screening of the spin vertex is also known as the Kanamori screening.

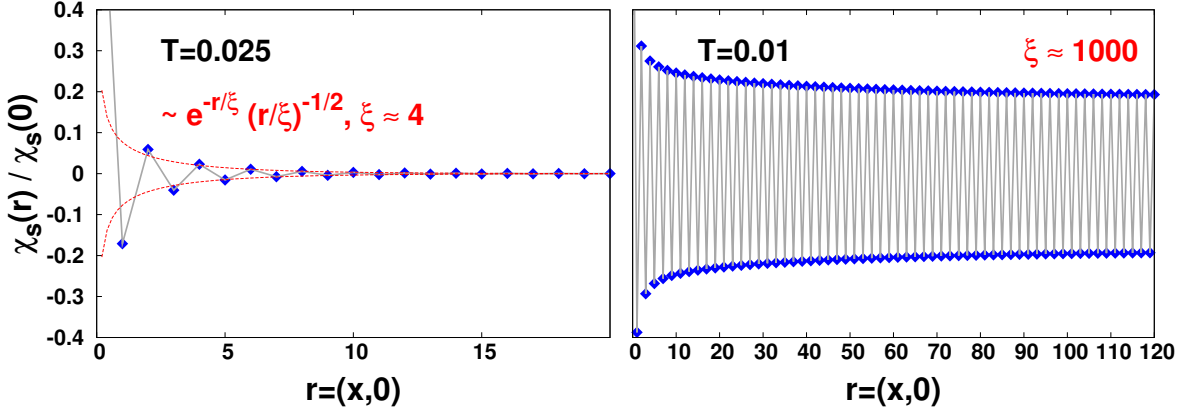


Fig. 14: Antiferromagnetic correlation function $\chi_{s,r}$ normalized to its $\mathbf{r} = 0$ value vs. distance \mathbf{r} for the two dimensional Hubbard model along the x -direction ($t' = t'' = 0$, $U = 0.5(4t)$; all energies are here in units of $4t$). The left and right panel show two different temperatures, $T = 0.025(4t)$ (left) and $T = 0.01(4t)$ (right), where largely different correlation lengths (ξ) are observed. From [15].

This reduction of the D Γ A spin susceptibility is key for a good description of antiferromagnetic spin-fluctuations which are hugely overestimated in RPA. In fact, it was shown that qualitatively and quantitatively the D Γ A susceptibility excellently agrees with other numerical calculations [31].

From the susceptibility one can obtain the correlation length ξ . Fourier-transformed to real space \mathbf{r} and time, the (equal-time) magnetic susceptibility behaves as

$$\chi_{sr} = \langle \mathbf{S}(\mathbf{r})\mathbf{S}(\mathbf{0}) \rangle \sim \left(\frac{|\mathbf{r}|}{\xi} \right)^{-1/2} e^{-\frac{|\mathbf{r}|}{\xi}} \quad (8)$$

at large distances \mathbf{r} . Here, $\mathbf{S}(\mathbf{r})$ denotes the spin operator of the electrons at position (lattice site) \mathbf{r} . Fig. 14 shows this spin-spin correlations or susceptibility of the Hubbard model. Clearly, an alternating (antiferromagnetic) correlation is visible. At high temperatures (left panel), the correlation length is short and correlations quickly decay. In two dimensions we get however an exponential increase of the correlation length with $1/T$ in D Γ A [15] which is the reason behind the very large correlation length of Fig. 14 (right panel). While a correlation length of $\xi = 4$ lattice sites (left panel) can still be covered in cluster extensions of DMFT and lattice quantum Monte Carlo methods, with the rapidly increasing correlation length at lower temperatures such cluster approaches reach their numerical limits.

At a three dimensional phase transition, the susceptibility diverges with critical exponent ν : $\xi \sim (T - T_c)^{-\nu}$, and similarly $\chi_{r,\mathbf{Q}\omega=0} \sim (T - T_c)^{-\gamma}$ with a critical exponent γ . These critical exponents could be calculated in D Γ A and DF for the first time for correlated electronic models, a topic that has been covered in a preceding Jülich Autumn School [14].

In practice, the correlation length is not calculated from fitting χ_{sr} . Instead one fits its Fourier-transform $\chi_{s,\mathbf{q}\omega=0}$ in momentum space. For large correlation lengths and in the vicinity of its

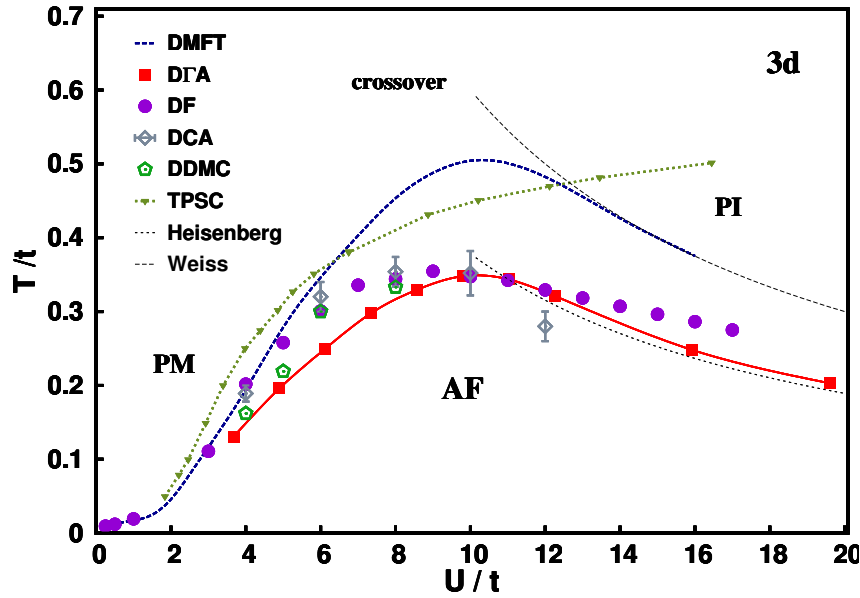


Fig. 15: Phase diagram of the half-filled three-dimensional Hubbard model on a cubic lattice with nearest-neighbor hopping t comparing various methods for the phase transition from the paramagnetic metallic (PM) and insulating (PI) phase to the antiferromagnetic insulating phase (AF). From [6] where further details and the abbreviation of the various methods can be found.

maximum at the dominating wave vector \mathbf{Q} ,⁹ the susceptibility is of the Ornstein-Zernike form

$$\chi_{s,\mathbf{q}\omega=0} \sim \frac{1}{(\mathbf{q}-\mathbf{Q})^2 + \xi^{-2}}. \quad (9)$$

That is, the inverse correlation length ξ^{-1} corresponds to the width of the susceptibility around its peak at $\mathbf{q} = \mathbf{Q}$.

In two dimensions, the Mermin-Wagner theorem is fulfilled and there is no long range antiferromagnetic order for finite temperature in the DΓA and diagrammatic extension of DMFT [6]. In three-dimensions the antiferromagnetic phase transition temperature T_c is reduced compared to DMFT, as shown in Fig. 15. Also the critical behavior in the vicinity of the phase transition is not any longer of mean-field type as in DMFT. Instead the critical exponents well agree¹⁰ with those of the Heisenberg model [6, 14] for half-filling, as to be expected from universality. Besides the susceptibility, spin-fluctuations also impact the electronic self-energy, as already indicated in Fig. 1. The effect F on the self-energy Σ can be directly calculated via the Schwinger-Dyson Eq. (4) [Fig. 6]. Physically, this corresponds to electron-(para)magnon scattering which can reduce the lifetimes of the quasiparticles.

A hallmark phenomenon of the effect of these spin-fluctuations on the self-energy is the opening of a pseudogap. Here, the self-energy is strongly momentum dependent. At the node, we have a Fermi liquid-like self-energy with a linear decay of self-energy at small frequencies, see Fig. 16. In contrast for the antinode we have an enhanced self-energy at small frequencies, which with decreasing temperatures develops a $1/\nu$ pole.

⁹For example, $\mathbf{Q} = (\pi, \pi)$ for the two-dimensional Hubbard model at half-filling.

¹⁰within the numerical error bars in the studied critical temperature regime

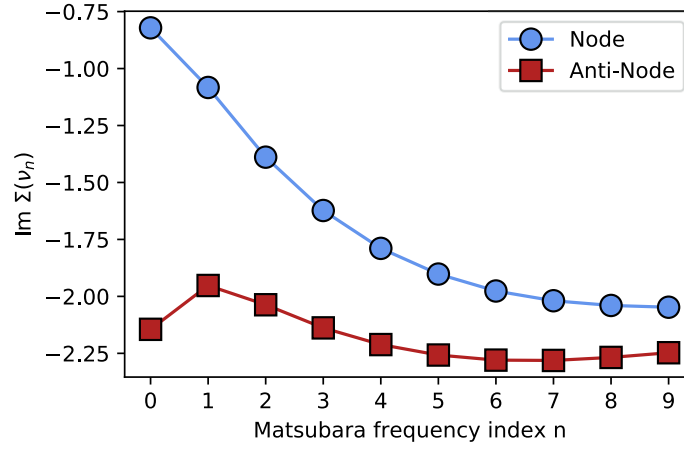


Fig. 16: Imaginary part of the DΓA self-energy vs. index n of the Matsubara frequency $\nu_n = i(2n+1)\pi T$, in the pseudogap region for a typical Hubbard model. Parameters: $U = 8$, $t' = -0.2$, $t'' = 0.1$, $T = 0.05$ (all in units of t), and 10% hole doping. Clearly the self-energy is very different for the two momenta plotted, i.e., in the nodal direction of the Fermi surface and in the anti-nodal direction. The downturn of the anti-nodal self-energy indicates the development of a pole and thus a splitting of the spectral function away from the Fermi energy. Figure by courtesy of Paul Worm.

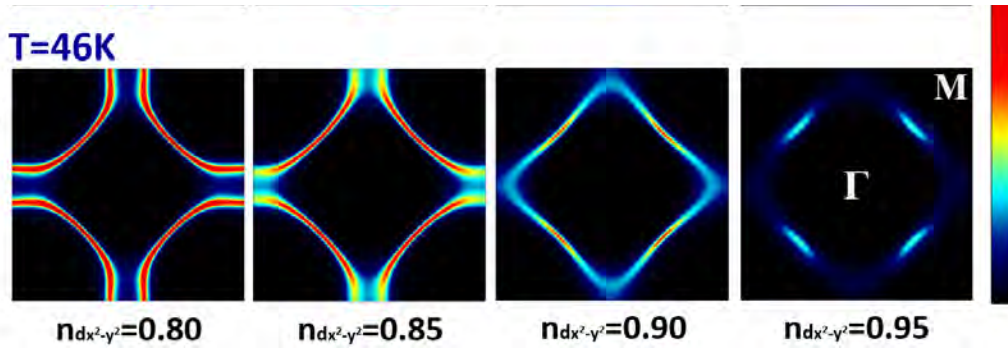


Fig. 17: DΓA spectrum at the Fermi energy for different dopings of nickelate superconductors throughout the Brillouin zone (i.e., x - and y -axis are the k_x and k_y momentum ranging from $-\pi$ to π , and the false color show the spectral function at the Fermi energy $\nu = 0$). From [30].

Turning to the infinite-layer nickelates, Fig. 17 shows the DΓA spectrum of the Ni $3d_{x^2-y^2}$ band¹¹ for nickelates as calculated by DΓA for the effective Hubbard model (see Sec. 4 where also the parameters can be found). The parent compound NdNiO₂, corresponding to $n_{3d_{x^2-y^2}} = 0.95$ (rightmost panel) has a pseudogap in the antinodal (PG) region, indicated by missing spectral weight in Fig. 17. This DΓA prediction still awaits an experimental confirmation.

For making nickelates superconducting, one needs to dope this $3d_{x^2-y^2}$ band, e.g., to $n_{3d_{x^2-y^2}} = 0.80$ or 0.85 . For these superconducting dopings, we have a clear Fermi surface throughout the Brillouin zone in Fig. 17 and no pseudogap.¹²

¹¹There are additional Nd pockets, see Sec. 4.

¹²As a technical remark, the spectrum has been calculated from $A_{\mathbf{k}\nu_0} = -G_{\mathbf{k}\nu_0}/\pi$ at the lowest Matsubara frequency $\nu_0 = i\pi T$, which leads to some additional broadening (smearing) but avoids the error-prone and cumbersome analytical continuation.

6 Superconductivity

Next we turn to the task of calculating the superconducting order and critical temperature T_c from the antiferromagnetic spin-fluctuations. The general procedure has already been indicated in Fig. 8(c). More specifically, the first step is the calculation of the full vertex F from Γ_{ph} (plus the crossing symmetrically related \overline{ph} channel), by summing the Bethe-Salpeter ladder diagrams in this channel(s). This calculation includes spin and charge fluctuations, but in the Hubbard model spin-fluctuations prevail. In the second step, we insert these spin-fluctuations into the pp channel. That is, we calculate $\Gamma_{pp} = \Lambda + \Phi_{ph} + \Phi_{\overline{ph}}$. Since no pp reducible diagrams have yet been included (except for the local ones), we can also rewrite this as $\Gamma_{pp} = F - \Phi_{pp}^{\text{local}}$. From this Γ_{pp} we can next recalculate F including superconducting fluctuations via the Bethe-Salpeter equation in the pp channel. This is akin to the Schwinger-Dyson Eq. (3) in the ph channel, except that we have to properly rotate the momenta and to use Γ_{pp} instead of Γ_{ph} . Similarly as in RPA [Eq. (7)], we get a superconducting (SC) susceptibility of the form

$$\chi_{SC, \mathbf{q}=0, \omega=0} = \sum_{kk'\nu\nu'} \underline{\underline{\chi^0}} \left(1 + \underline{\underline{\Gamma_{pp, \mathbf{q}=0, \omega=0}}} \underline{\underline{\chi^0}} \right)^{-1}. \quad (10)$$

Here, we are interested in the instability at $\omega = 0$ and the coupling of two fermions with momentum \mathbf{k} and $-\mathbf{k}$ into a Cooper pair as in Fig. 8(c), i.e., a total momentum $\mathbf{q} = 0$ in the pp channel.¹³ The generalized¹⁴ bare bubble susceptibility at $\omega = 0$ and $\mathbf{q} = 0$ is

$$\chi_{\mathbf{k}\mathbf{k}'\nu\nu'}^0 = G_{\mathbf{k}'\nu'} G_{-\mathbf{k}-\nu} \delta(\mathbf{k} - \mathbf{k}') \delta_{\nu, \nu'} \quad (11)$$

and the double underlines denote matrices with respect to $\mathbf{k}\nu$ and $\mathbf{k}'\nu'$.

In order to obtain superconductivity, i.e., a diverging $\chi_{SC, \mathbf{q}=0, \omega=0}$ one of the eigenvalues λ of the matrix $-\underline{\underline{\Gamma_{pp, \mathbf{q}=0, \omega=0}}} \underline{\underline{\chi^0}}$ has to approach $\lambda = 1$. For electron-phonon mediated superconductivity this is simple since the electron-phonon coupling gives rise to an attractive (negative) Γ_{pp} . For the repulsive Hubbard model, this is much more difficult to achieve since Γ_{pp} also includes the repulsive (positive) Coulomb interaction $+U$. Nonetheless, an attraction can be mediated by antiferromagnetic spin-fluctuations through retardation (ν, ν') and non-locality (k, k'). The k, k' structure of the diverging ($\lambda \rightarrow 1$) eigenvector (or the corresponding real space structure) determines the symmetry of the superconducting symmetry breaking and gap (s -wave, d -wave etc.). For phonons with an across the board attraction, one gets s -wave superconductivity. For the spin-fluctuations in the Hubbard model d -wave is more favorable to avoid the large local repulsion $+U$.¹⁵

In an infinitely-extended strictly two-dimensional system there is no superconductivity at finite temperatures. Instead, a finite temperature topological Berezinskii-Kosterlitz-Thouless (BKT)

¹³This \mathbf{q} is not to be confused with that in the ph channel which is peaked around $\mathbf{Q} = (\pi, \pi)$ and corresponds to another combination of the external legs of the four-point vertex F .

¹⁴without $kk'\nu\nu'$ summation

¹⁵For the d -wave, Γ_{pp} mediates between momenta \mathbf{k} and \mathbf{k}' on the Fermi surface, for which the superconducting eigenvalue has opposite sign.

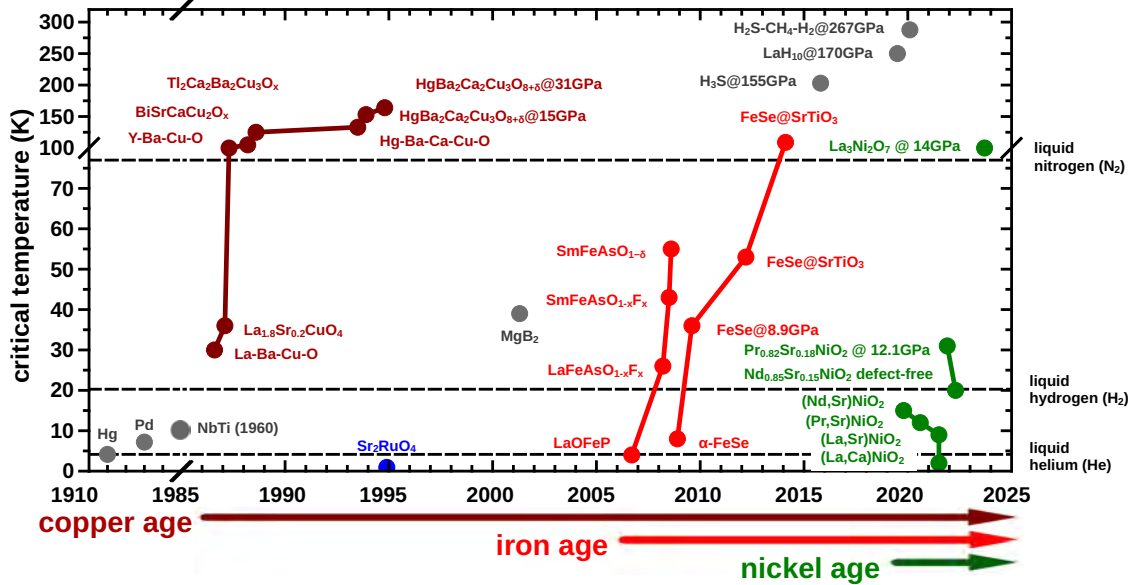


Fig. 18: Superconducting T_c vs. year of discovery for various important superconductors. After the copper age, there came an iron age, and now we are in the nickel age. From [33] (updated).

transition is possible. At first glance, this is a contradiction to the observed superconductivity in cuprates and nickelates. However, these materials are not perfectly two-dimensional but layered quasi-two-dimensional materials. In this situation, and with the strongly increasing correlation length around the BKT transition, even a tiny coupling in the inter-layer direction will trigger superconductivity, a little bit below the BKT transition. In the D Γ A calculation, a self-consistency is necessary to (possibly) get a BKT transition. Without the self-consistent feedback of the superconducting fluctuations, we eventually get a mean-field kind of superconducting transition and a finite T_c which is closer to experiment than the ideal two-dimensional calculation with a BKT transition.

As for superconducting materials, the nickelate superconductors [32] have led to enormous theoretical and experimental efforts. One therefore also speaks of the nickel age for superconductivity, see Fig. 18.

Also shown are hydrogen-based superconductors that are phonon-mediated and have a T_c close to room temperature, but only under the enormous pressure of a diamond anvil cell. Hence the challenge is to increase T_c for the unconventional (i.e., not phonon-mediated) correlated superconductors or to reduce the pressure for the hydrogen-based superconductors. Here, the nickelates have a T_c that is still quite substantially below that of the cuprates. However, one can expect T_c to further increase somewhat with new and better synthesized nickelate films. For example, T_c above 30 K was demonstrated recently for infinite-layer nickelates [34]. The high hope is that infinite-layer nickelates and cuprates, being very similar but also decisively distinct, put us in the ideal situation to discriminate the essentials from the incidentals for high-temperature superconductivity. The iron pnictides and Ruddlesden-Popper nickelates are instead pretty far away from the cuprate or nickelate physics with their imminent multi-orbital physics.

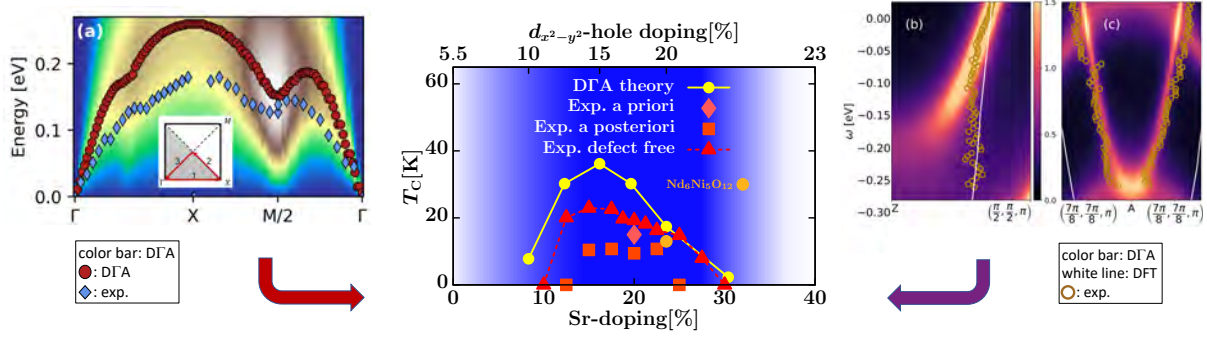


Fig. 19: Center: Superconducting T_c vs. doping x of $\text{Sr}_x\text{Nd}_{1-x}\text{NiO}_2$ as predicted by DΓA [30] and “a posteriori” [35] confirmed experimentally; the agreement further improved after synthesizing “defect free” films [36]. “A priori” [32] a single nickelate superconductor was known. The T_c of $\text{Nd}_6\text{Ni}_5\text{O}_{12}$ aligns as well [37, 38]. More recently, also the underlying spin-fluctuations and one-electron states were found to agree excellently with resonant inelastic x-ray scattering (RIXS, left) [39, 40] and angular-resolved photoemission spectroscopy (ARPES, right) [41–43]. As these enter the calculation of T_c , indicated by the arrows, this gives us altogether a high level of confidence that the modeling is correct and accurate. (Note, the experimental ARPES dispersion is from the 2nd derivative, which also shows waterfalls in the theory [43, 44].) For such a notoriously difficult to determine quantity as the superconducting T_c and without adjustable parameters, the accuracy is indeed astonishing.

In Sec. 4, we have already pointed out that the nickelates can be described by a one-band Hubbard model with an approximately adjusted doping; and in Fig. 17 we have shown the thus calculated spectrum with a pseudogap for the (non-superconducting) parent compound NdNiO_2 . For this nickelate Hubbard model, we find [30] (not surprisingly) d -wave superconductivity in ladder DΓA. The superconducting T_c vs. doping is plotted in Fig. 19 as a function of Sr-doping. Actually the theoretical calculation was a prediction here since, when three years ago superconductivity in nickelates has been discovered [32], only a single T_c at 20% doping was available at first because of the difficulties to synthesize $\text{Nd}_{1-x}\text{Sr}_x\text{NiO}_2$ in the low oxidation state Ni^{+1} . With the recent progress to synthesize clean superconducting nickelate films [36], the theoretical predicted phase diagram has been spectacularly confirmed in experiment, see Fig. 19. Also the strength of spin-fluctuations that were found to mediate superconductivity in DΓA and the one-particle electron spectrum were predicted correctly, see Fig. 19 left and right panel, respectively. This provides altogether a high level of confidence that we have achieved an excellent modeling of infinite-layer nickelates, using a novel methodology for the calculation of strongly correlated superconductors.

The physical reason that we see in Fig. 19 a superconducting dome is two-fold: The downturn at large doping is because antiferromagnetic spin-fluctuations get weaker the further we are away from half-filling. The down-turn at small doping, towards half-filling, on the other hand is a consequence of the pseudogap which develops in this doping region, see Fig. 17. Thus, the electron propagators in Fig. 8(c) lose coherence in a larger part of the Fermi surface, and the superconducting susceptibility is suppressed despite considerable spin-fluctuations.

Recently also finite-layer variants of the infinite-layer nickelate superconductor have been synthesized [37]. These have very similar hopping parameters and physics [38,45]. Their T_c agrees with D Γ A as well [38,45] (and with the T_c of the infinite layer nickelates shown in Fig. 19). Here, DMFT indicates that, if we only have a few layers, finite-layer nickelates have no pockets. This is confirmed by a—in contrast to infinite-layer nickelates—positive (hole-like) hall resistivity [37]. The absence of pockets also further corroborates the picture of a decoupled reservoir that is not relevant for superconductivity as advocated in Fig. 9. Altogether the DFT+DMFT and D Γ A calculations for nickelates and the experiments for the different nickelates provide for a consistent picture [38]. This gives us some hope that we might finally be able to actually calculate and predict superconducting T_c 's, the arguably biggest challenge of solid state theory.

7 Conclusion and outlook

Diagrammatic extensions of DMFT are very appealing in several ways: They combine the good description of DMFT with the, to the best of our knowledge, most important non-local physics. In this chapter we have focused on spin-fluctuations and how they mediate superconductivity, but other fluctuations such as charge fluctuations, weak localization corrections, excitons—you name it—are treated on an equal footing. Also (quantum) criticality can be described, a topic that has been discussed in an earlier Jülich Autumn School [14]. Diagrammatic extensions of DMFT are also very appealing since they marry quantum field theoretical with its qualitative understanding and numerics which is unavoidable for a quantitative description of strongly correlated electrons systems.

Different variants of diagrammatic extensions of DMFT exist, and for the sake of brevity we have concentrated here on the first (and widely employed) variant: the dynamical vertex approximation. All variants have in common that they calculate a local vertex and construct non-local correlations from this vertex diagrammatically. In regions of the phase diagram where non-local correlations are short range, results are similar to those from cluster extensions of DMFT. However, the diagrammatic extensions also offer the opportunity to study long-range correlations, which is key for (quantum) criticality but also important in other situations, as well as to calculate materials with many orbitals [17].

There is still plenty of room for improvement: starting from (i) various self-consistencies, using (ii) a clusters instead of a single site as a starting point [46], (iii) compactifying the vertex with various methods such as the intermediate representation (IR) in frequency space [23], quantics tensor trains (see Chapter “Learning Feynman Diagrams with Tensor Trains” by X. Waintal [3]), the truncated unity in momentum space [22], and the single-boson exchange [24] in Feynman diagram space. The hope is that the reduced memory burden then allows parquet D Γ A calculations at lower temperatures or with multi orbitals. Another development has been (iv) the calculation of the underlying two-particle vertices directly for real frequencies, which is possible using the numerical renormalization group (NRG) method, see Chapter “The physics of quantum impurity models” by J. von Delft in 2022 [4].

In this chapter, we have concentrated on antiferromagnetic spin-fluctuations and how they me-

diate superconductivity. The T_c predicted for nickelates well agrees with experiment—actually much better than what we dared to hoped for. This gives us some confidence that we are on the right track to better model and understand superconductivity, that we eventually have the tools to predict T_c for new materials. While many theoreticians in the many-body community consider antiferromagnetic spin-fluctuations to be at the origin of high temperature superconductivity, the mechanism for unconventional superconductivity remains hotly debated. Maybe through a careful analysis and predictions we can now prove that this is indeed the microscopic mechanism for high-temperature superconductivity.

Diagrammatic extensions of DMFT such as the D Γ A also offer the opportunity to study many other phenomena and to do material calculations. This leaves plenty of opportunities for the next generation of physicists.

Acknowledgment First of all, I would like to thank my co-workers on the research presented here, Oleg Janson, Andrey Katanin, Anna Kauch, Motoharu Kitatani, Jan M. Tomczak, Liang Si, Alessandro Toschi, and Paul Worm. Without them, the success of diagrammatic extensions of DMFT would not have been possible. Finally, I gratefully acknowledge financial support by the Austrian Science Fund (FWF) through project Grant DOI 10.55776/I5398, 10.55776/36213 and the Research Unit QUAST of German Science Foundation (DFG) (DFG FOR5249; Austrian part financed through FWF project Grant DOI 10.55776/I5868).

References

- [1] W. Metzner and D. Vollhardt, Phys. Rev. Lett. **62**, 324 (1989)
- [2] A. Georges and G. Kotliar, Phys. Rev. B **45**, 6479 (1992)
- [3] E. Pavarini, E. Koch, D. Vollhardt, and A.I. Lichtenstein (eds.):
Understanding Correlated Materials with DMFT,
Modeling and Simulations, Vol. 15 (Forschungszentrum Jülich, 2025)
<http://www.cond-mat.de/events/correl22>
- [4] E. Pavarini, E. Koch, D. Vollhardt, and A.I. Lichtenstein (eds.):
Dynamical Mean-Field Theory of Correlated Electrons,
Modeling and Simulations, Vol. 12 (Forschungszentrum Jülich, 2022)
<http://www.cond-mat.de/events/correl22>
- [5] A. Schiller and K. Ingersent, Phys. Rev. Lett. **75**, 113 (1995)
- [6] G. Rohringer, H. Hafermann, A. Toschi, A.A. Katanin, A.E. Antipov, M.I. Katsnelson, A.I. Lichtenstein, A.N. Rubtsov, and K. Held, Rev. Mod. Phys. **90**, 025003 (2018)
- [7] T. Maier, M. Jarrell, T. Pruschke, and M.H. Hettler, Rev. Mod. Phys. **77**, 1027 (2005)
- [8] K. Held, A. Katanin, and A. Toschi, Prog. Theor. Phys. (Suppl.) **176**, 117 (2008)
- [9] A. Toschi, A.A. Katanin, and K. Held, Phys. Rev. B **75**, 045118 (2007)
- [10] A.N. Rubtsov, M.I. Katsnelson, and A.I. Lichtenstein, Phys. Rev. B **77**, 033101 (2008)
- [11] T.A. Maier, M.S. Jarrell, and D.J. Scalapino, Phys. Rev. Lett. **96**, 047005 (2006)
- [12] T. Ribic, P. Gunacker, S. Isakov, M. Wallerberger, G. Rohringer, A.N. Rubtsov, E. Gull, and K. Held, Phys. Rev. B **96**, 235127 (2017)
- [13] P. Kappl, T. Ribic, A. Kauch, and K. Held, arXiv:2412.01848.
- [14] K. Held: *Quantum criticality and superconductivity in diagrammatic extensions of DMFT*, in E. Pavarini and E. Koch and D. Vollhardt and A.I. Lichtenstein (eds.):
DMFT: From Infinite Dimensions to Real Materials,
Modeling and Simulations, Vol. 8 (Forschungszentrum Jülich, 2018)
<http://www.cond-mat.de/events/correl18>
- [15] T. Schäfer, F. Geles, D. Rost, G. Rohringer, E. Arrigoni, K. Held, N. Blümer, M. Aichhorn, and A. Toschi, Phys. Rev. B **91**, 125109 (2015)
- [16] A. Kauch, P. Pudleiner, K. Astleithner, P. Thunström, T. Ribic, and K. Held, Phys. Rev. Lett. **124**, 047401 (2020)

- [17] A. Galler, P. Thunström, P. Gunacker, J.M. Tomczak, and K. Held, Phys. Rev. B **95**, 115107 (2017)
- [18] M. Kitatani, R. Arita, T. Schäfer, and K. Held, arXiv:2203.12844
- [19] N.E. Bickers: *Theoretical Methods for Strongly Correlated Electrons* (Springer, Heidelberg, 2004), chap. 6, pp. 237–296
- [20] M. Wallerberger, A. Hausoel, P. Gunacker, A. Kowalski, N. Parragh, F. Goth, K. Held, and G. Sangiovanni, Comp. Phys. Commun. **235**, 388 (2019)
- [21] P. Gunacker, M. Wallerberger, E. Gull, A. Hausoel, G. Sangiovanni, and K. Held, Phys. Rev. B **92**, 155102 (2015)
- [22] C.J. Eckhardt, C. Honerkamp, K. Held, and A. Kauch, Phys. Rev. B **101**, 155104 (2020)
- [23] M. Wallerberger, H. Shinaoka, and A. Kauch, Phys. Rev. Res. **3**, 033168 (2021)
- [24] F. Krien, A. Valli, and M. Capone, Phys. Rev. B **100**, 155149 (2019)
- [25] J. Kaufmann, C. Eckhardt, M. Pickem, M. Kitatani, A. Kauch, and K. Held, Phys. Rev. B **103**, 035120 (2021)
- [26] T. Ayral and O. Parcollet, Phys. Rev. B **94**, 075159 (2016)
- [27] M. Kitatani, T. Schäfer, H. Aoki, and K. Held, Phys. Rev. B **99**, 041115 (2019)
- [28] K. Held, L. Si, P. Worm, O. Janson, R. Arita, Z. Zhong, J.M. Tomczak, and M. Kitatani, Front. Phys. **9** (2022)
- [29] H. Sun *et al.*, Nature **621**, 493 (2023)
- [30] M. Kitatani, L. Si, O. Janson, R. Arita, Z. Zhong, and K. Held, npj Quantum Mater. **5**, 59 (2020)
- [31] T. Schäfer *et al.*, Phys. Rev. X **11**, 011058 (2021)
- [32] D. Li, K. Lee, B.Y. Wang, M. Osada, S. Crossley, H.R. Lee, Y. Cui, Y. Hikita, and H.Y. Hwang, Nature **572**, 624 (2019)
- [33] L. Si, P. Worm, and K. Held, Crystals **12** (2022)
- [34] S. Lin Er Chow, Z. Luo, and A. Ariando, Nature **642**, 58 (2025)
- [35] D. Li, B.Y. Wang, K. Lee, S.P. Harvey, M. Osada, B.H. Goodge, L.F. Kourkoutis, and H.Y. Hwang, Phys. Rev. Lett. **125**, 027001 (2020)
- [36] K. Lee *et al.*, Nature **619**, 288 (2023)

- [37] G.A. Pan *et al.*, Nat. Mater. **21**, 160 (2022)
- [38] P. Worm, L. Si, M. Kitatani, R. Arita, J.M. Tomczak, and K. Held, arXiv:2111.12697
- [39] H. Lu *et al.*, Science **373**, 213 (2021)
- [40] P. Worm *et al.* Phys. Rev. B **109**, 235126 (2024)
- [41] W. Sun *et al.*, Sci. Adv. **11**, eadr5116 (2025)
- [42] X. Ding *et al.*, Natl. Sci. Rev. **11**, nwae194 (2024)
- [43] L. Si, E. Jacob, W. Wu, A. Hausoel, J. Krsnik, P. Worm, S.D. Cataldo, O. Janson, K. Held, Phys. Rev. Res. **6**, 043104 (2024)
- [44] J. Krsnik and K. Held, Nat. Comm. **16**, 255 (2025)
- [45] A. Hausoel, S. Di Cataldo, M. Kitatani, O. Janson, and K. Held, arXiv:2502.12144
- [46] D. Kiese, N. Wentzell, I. Krivenko, O. Parcollet, K. Held, and F. Krien, Phys. Rev. Res. **6**, 043159 (2024)